46th AIAA Aerospace Sciences Meeting and Exhibit
7 - 10 January 2008, Reno, Nevada

AIAA 2008-1069

Numerical simulation of laser–induced breakdown in air

Shankar Ghosh* and Krishnan Mahesh†

University of Minnesota, Minneapolis, MN, 55455, USA

Numerical simulations of laser energy deposition in quiescent air and in isotropic turbulence are conducted. The flow field is classified into three phases: shock formation, shock propagation and subsequent collapse of the plasma core. Each phase is studied in detail. Vorticity is found to be generated in the flow at short times due to baroclinic effects and at long times due to rolling up of the plasma core. An explanation is presented for the roll up process. Scaling analysis is performed for different amounts of laser energy deposited and different Reynolds number of the flow. Simulations are conducted using three different models for air based on different levels of physical complexity. The impact of these models on the evolution of the flow field is discussed.

I. Introduction

When a laser beam is focused onto a gas, the molecules in the focal volume absorb radiation from the laser source. The intensity of the incident laser radiation can be increased by using a converging lens and hence very high temperatures can be achieved. The molecules in the focal volume undergo a number of reactions resulting in formation of a plasma. This phenomenon is known as laser–induced breakdown of a gas. At the end of the plasma formation process, a tear–drop shaped energy spot with temperature and pressure higher than that of the surroundings is obtained. The resulting gradients in pressure lead to the formation of a strong blast wave that propagates into the background. Also the core of the plasma region rolls up in time and forms a toroidal vortex ring.

Laser–induced breakdown has been studied by a number of workers (e.g. Maker et al. 1963, Damon & Tomlinson 1963, Meyerand & Haught 1963, Root 1989, Knight 2003), and finds application in localized flow control of supersonic flows (Adelgren et al. 2003, Shneider et al. 2003), drag reduction in supersonic and hypersonic flows (Riggins 1999), ignition of combustion gases (Phuoc 2000) and providing thrust to aerospace vehicles (Molina-Morales et al. 2001, Wang et al. 2001).

Theoretical studies of the laser–induced breakdown process have been conducted by Zeldovich and Raizer (1965), Raizer (1966) and Kroll and Watson (1972). Recent experiments on laser–induced breakdown include Ditmire et al. (1997), Parigger et al. (1995 a, b), Yalcin et al. (1999), Jiang et al. (1999), Lewis et al. (1999), Chen et al. (2000), Adelgren et al. (2001) and Glumac et al. (2005). Jiang et al. (1998) focused a laser beam of $1.38J$ on a $3mm$ diameter spherical region to cause breakdown of air. The laser was pulsed for a duration of 18 nanoseconds. Adelgren et al. (2001) pulsed a Nd:YAG laser of $200mJ$ for 10 nanoseconds in air.

Laser–induced breakdown is a complicated process involving coupling between particle–electromagnetic wave interaction, chemical reactions and fluid dynamic effects. However, experimental data show a wide separation in time–scales of the laser pulse duration and blast wave propagation: i.e. the laser is pulsed on a time–scale of 10 nanoseconds while the blast wave is observed on a time–scale of 10 to 100 microseconds. Since the

*Graduate Research Assistant
†Associate Professor

plasma forms on the time–scale of the laser pulse duration, there is a three to four order of magnitude separation in time–scale. The plasma may therefore be assumed to form instantaneously, to evaluate its gas–dynamic effect on the surrounding fluid.

Various simulation models have been used to understand different features of this phenomenon. Brode (1955) performed a numerical simulation of the blast wave and concluded that the ideal gas assumption was reasonable for shock pressures less than 10 atmospheres in air. Steiner et al. (1998) perform computations using a real gas model to show that when initialized with a self similar strong shock solution, the shock radius in the real gas model is quite close to that predicted by the classical point source explosion in an ideal gas. Other computations of blast wave propagation in quiescent air include those by Jiang et al. (1998) and Yan et al. (2003). Dors et al. (2000, 2003) present a computational model which considers the asymmetry of laser energy deposition as well as ionization and dissociation effects on fluid properties. The initial stages of plasma formation due to laser energy deposition were modeled by Kandala and Candler (2005). Very few simulations account for the physical tear–drop shape of the plasma. Even simulations with very complex physical models do not show very prominent flow features observed in experiment. One of the objectives of this paper is to investigate the level of physical complexity required to simulate accurately the flow features observed in the experiments. Also most of the past work have studied laser–induced plasma generation in laminar flows. One of the objectives of this paper is to study the effect of laser energy deposition on isotropic turbulence.

Our past work (Ghosh and Mahesh 2007) has considered simulating laser–induced plasma in air using ideal gas equations with transport properties as functions of temperature. The flow field resulting from laser induced breakdown was divided into shock formation, shock propagation and subsequent roll up of the plasma core. Vorticity is found to be generated at short and long times through different mechanisms. For the turbulent simulations, turbulence levels were found to get amplified in the vicinity of the plasma core due to mean compression. This paper considers simulation of laser–induced plasma in air using three different models for air involving different levels of physical complexity. The different stages of the flow field evolving as a result of laser energy deposition is described in more detail. An explanation is provided to describe the process of rolling up of the plasma core. Scaling analysis is performed for different values of T_0 and the Reynolds number of the flow. The effect of the different simulation models on the initial conditions, time evolution of the mean flow and resulting amplification of the background turbulence levels is described in detail.

II. Physical Model

The Navier–Stokes equations are used to simulate the flow–field resulting from the deposition of laser energy in air. Local thermodynamic equilibrium conditions are assumed to apply. Also, radiation losses after formation of the plasma spot are assumed to be negligible. Hence, the governing equations do not have additional source terms. The continuity and compressible Navier–Stokes equations are given by

$$\frac{\partial \rho}{\partial t} + \frac{\partial \rho u_i}{\partial x_i} = 0, \tag{1}$$

$$\frac{\partial \rho u_j}{\partial t} + \frac{\partial \rho u_j u_i}{\partial x_i} = -\frac{\partial}{\partial x_i}\left[p\delta_{ij} - \frac{\mu}{Re}\left(\frac{\partial u_i}{\partial x_j} + \frac{\partial u_j}{\partial x_i} - \frac{2}{3}\frac{\partial u_k}{\partial x_k}\delta_{ij}\right)\right], \tag{2}$$

$$\frac{\partial \rho e_T}{\partial t} + \frac{\partial \rho e_T u_i}{\partial x_i} = \frac{\partial}{\partial x_i}\left[-pu_i + \frac{\mu}{Re}\left(\frac{\partial u_i}{\partial x_j} + \frac{\partial u_j}{\partial x_i} - \frac{2}{3}\frac{\partial u_k}{\partial x_k}\delta_{ij}\right)u_j\right] + \frac{\partial}{\partial x_i}\left(\frac{\kappa}{(\gamma-1)RePr}\frac{\partial T}{\partial x_i}\right) \tag{3}$$

where all the variables are non–dimensionalized by their initial background values.

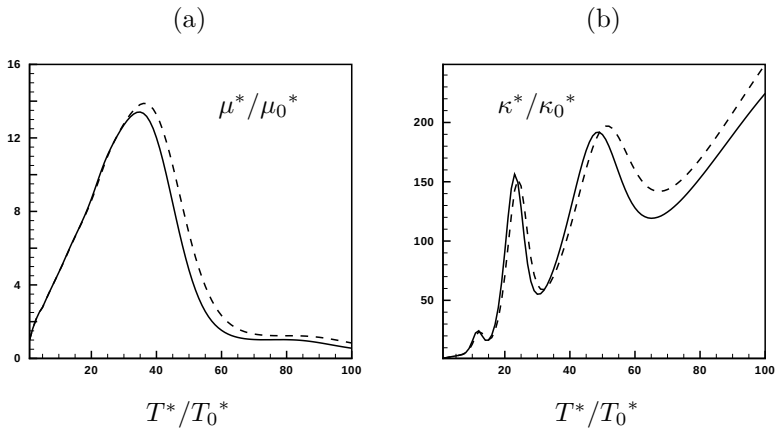

Figure 1. (a) Variation of the coefficient of viscosity μ with temperature T and pressure p, (b) Variation of the coefficient of thermal conductivity κ with temperature T and pressure p, ——— : $p = 1atm.$, - - - - : $p = 10atm.$

$$
\begin{aligned}
x_i = x_i{}^*/L_0{}^*, \qquad u_i = u_i{}^*/c_0{}^*, \qquad t = t^* c_0{}^*/L_0{}^*, \\
\rho = \rho^*/\rho_0{}^*, \qquad p = p^*/\rho_0{}^* c_0{}^{*2}, \qquad T = T^*/T_0{}^* \\
\mu = \mu^*/\mu_0{}^*, \qquad \kappa = \kappa^*/\kappa_0{}^*.
\end{aligned} \tag{4}
$$

Here, the subscript '0' denotes initial background values and the superscript, '*' denotes dimensional variables. L_0^* is the reference length scale and is obtained by comparing the non–dimensional length of the plasma region used in the simulations to the physical length of the plasma. c_0^* is the speed of sound based on initial background temperature; i.e.

$$c_0{}^* = (\gamma R^* T_0{}^*)^{1/2}. \tag{5}$$

The Reynolds number and Prandtl number are defined as

$$Re = \rho_0{}^* c_0{}^* L_0{}^*/\mu_0{}^*; \quad Pr = \mu^* c_p{}^*/k^*. \tag{6}$$

Simulations are conducted using models with three different levels of physical complexity. These models are described below.

A. Model 1

For the simplest case, the effects of chemical reactions resulting from high temperatures in the flow are neglected. Ideal gas relations are used to represent the thermodynamic properties of air. Simple constitutive relations are assumed for the transport properties.
The coefficient of viscosity is described by the power law $\mu = T^{0.67}$, the coefficient of thermal conductivity is obtained by assuming a constant Prandtl number of 0.7 and γ is assumed to be 1.4. The nondimensionalized equation of state becomes

$$p = \rho T/\gamma, \tag{7}$$

where the temperature is related to the internal energy by the relation

$$T = \gamma(\gamma - 1)e, \tag{8}$$

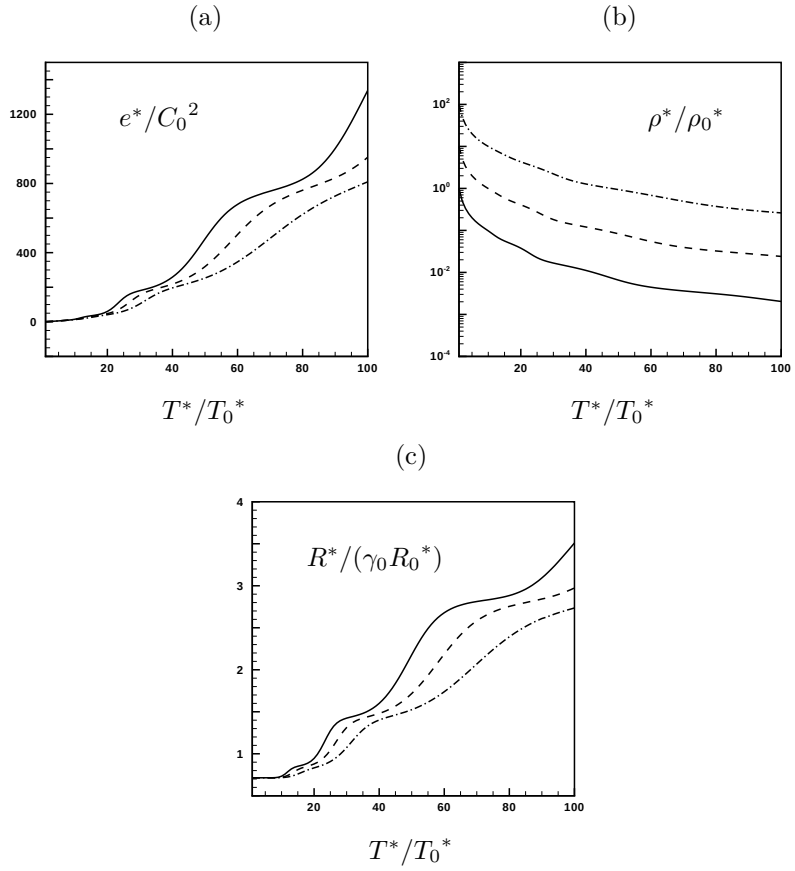

Figure 2. (a) Variation of internal energy e with temperature T and pressure p, (b) Variation of density ρ with temperature T and pressure p, (c) Variation of R with temperature T and pressure p, ——— : $p = 1atm.$, - - - - : $p = 10atm.$, —·— : $p = 100atm.$

and the total energy is related to internal energy and kinetic energy as

$$\rho e_T = \rho e + \frac{1}{2}\rho u_i u_i. \tag{9}$$

To obtain the initial conditions, a three dimensional temperature profile is used to represent the effect of localized laser energy addition. Since the energy addition is on a very fast time scale, it is assumed that the density does not change significantly. Thus the initial pressure profile can be obtained using equation 7 and the internal energy e is obtained using equation 8. At the end of every time–step, pressure and temperature are obtained from the conserved variables using the above constitutive equations.

B. Model 2

This model considers the effect of chemical reactions resulting in dissociation, ionization and recombination of different species. Thermodynamic and transport properties for air are computed up to a temperature of $30,000\ K$. An 11 species model for air is considered namely

$$N_2,\ O_2,\ NO,\ N,\ O,\ {N_2}^+,\ {O_2}^+,\ NO^+,\ N^+,\ O^+ \text{ and } e^-,$$

and the composition of the individual species are obtained using the law of mass action. Then the mixture properties are obtained as a function of temperature based on the composition of the individual species.

These properties are validated against data from the NASA code CEA. Also the properties are computed for different values of pressure ranging from 1 atmosphere to 300 atmospheres. However model 2 uses data computed for a pressure of 1 atmosphere only, i.e. it ignores the variation of these properties with pressure. The speed of sound based on initial background temperature is given by

$$c_0{}^* = (\gamma_0 R_0{}^* T_0{}^*)^{1/2}. \tag{10}$$

The dimensional coefficients of viscosity and thermal conductivity $\mu(T)^*$ and $\kappa(T)^*$ are shown in figure 1. The equation of state in nondimensional form is now written as

$$p = \rho R(T) T, \tag{11}$$

where

$$R(T) = R^*(T)/\gamma_0 R_0, \tag{12}$$

and the variation of R^* with temperature is shown in figure 2c. The total energy is related to internal energy and kinetic energy through equation 9 and temperature is obtained from internal energy using the equilibrium dependence of internal energy on temperature shown in figure 2a. The Reynolds number and Prandtl number are given by

$$Re = \rho_0{}^* c_0{}^* L_0{}^* / \mu_0{}^*, \quad Pr = \mu_0{}^* c_{p0}{}^* / \kappa_0{}^*. \tag{13}$$

The initial pressure profile is obtained using $\rho = \rho_0$ in equation 11 and data for variation of R with temperature. The internal energy e is then obtained from the value of temperature (figure 2a) using cubic spline interpolation. The total energy is related to internal energy and kinetic energy through equation 9. At the end of every time–step, temperature is obtained from values of e using data shown in figure 2a. Once the temperature field is known, the pressure field is obtained as before.

C. Model 3

Model 3 takes into account the effects of pressure variation on the properties. Pressures in the flow are quiet high at initial times and so the pressure variation of the thermodynamic properties can have a notable effect on the flow field. In particular, the effect on the initial conditions could be significant. The equation of state is given by

$$p = \rho R(T, p) T, \tag{14}$$

where

$$R(T, p) = R^*(T, p)/(\gamma_0 R_0{}^*), \tag{15}$$

and the variation of R with temperature and pressure is shown in figure 2c. The initial pressure is obtained through a process of iteration using $\rho = \rho_0$ in equation 14 and data for variation of R with pressure and temperature. The internal energy e is then obtained from the values of pressure and temperature (figure 2a). The total energy is related to internal energy and kinetic energy through equation 9. At the end of every time–step, pressure and temperature are obtained from the values of ρ and e using the equilibrium data for $e(T, p)$ and $\rho(T, p)$ shown in figure 2.

III. Numerical Model

A. Fourier discretization

The Navier–Stokes equations are solved using Fourier methods to compute the spatial derivatives. A collocated approach is used, and the solution is advanced in time using a fourth order Runge–Kutta scheme. The skew–symmetric form of the convection terms is used to suppress aliasing errors resulting from the nonlinear convection terms (Blaisdell 1991). The above algorithm is implemented for parallel platforms using MPI. The library FFTW is used to compute Fourier transforms, and a pencil data structure is used. Each processor stores data along the entire extent of the x_1- direction, while data along the x_2- and x_3- directions are equally distributed among the processors. Fourier transforms along the x_1- direction are therefore readily computed, while transforms in the other directions require that the data be transposed prior to transforming. The solver assumes periodic boundary conditions. The flow field resulting from laser energy deposition is axisymmetric and non–stationary in time. The periodic boundary conditions are valid as long as the blast wave does not reach the domain boundaries. This is because if the blast wave is well resolved, the gradients ahead of it will be zero. The continuity equation is solved using logarithm of density as a variable instead of density to ensure stability in regions of very low density in the plasma core.

B. Shock capturing

Recall that a strong shock wave propagates through the flow domain, when energy is added instantaneously. Experiments in laser induced breakdown (Yan et al 2003) show that the maximum temperature in the core is very high. This leads to sharp gradients in the flow variables. Since the flow solver uses spectral methods for spatial discretization, resolving these sharp gradients requires a highly refined mesh. The computational cost therefore increases significantly with increasing core temperatures. The Fourier spectral method is therefore combined with a shock capturing scheme proposed by Yee et al (1999), to avoid resolution of the shock thickness.

The shock capturing scheme is based on the finite volume methodology, and is applied as a corrector step to the Fourier discretization used in this paper. In the first step, the predicted form of the solution vector is obtained using Fourier methods as discussed in section III, subsection A. This solution vector is then corrected using the filter numerical fluxes obtained by using a characteristic based filter. The filter numerical flux vector is of the form

$$\widetilde{F}^{\star}_{i+1/2,j,k} = \frac{1}{2} R_{i+1/2,j,k} \phi^{\star}_{i+1/2,j,k} \tag{16}$$

where R is the right eigen vector matrix. The elements of $\phi^{\star}$ are denoted by $\phi^{l\star}$ and are given by

$$\phi^{l\star}_{i+1/2,j,k} = \kappa \theta^{l}_{i+1/2,j,k} \phi^{l}_{i+1/2,j,k} \tag{17}$$

The parameter κ is problem dependent and lies between 0.03 and 2 (Yee et al 1999). $\kappa = 1.0$ has been used in the simulations. The function $\theta^{l}_{i+1/2,j,k}$ is the Harten switch (Harten 1978) and depends on the left eigen vector matrix L. The formulation used for $\phi^{l}_{i+1/2,j,k}$ is given by the Harten–Yee upwind TVD form (Yee et al 1999).

However for high temperature flows, in order to remain consistent with the numerical method used for the predictor step, separate treatment needs to be provided to the computation of the eigen vector matrices R and L. The specific heats at constant pressure and volume C_P and C_V are no longer constants but depend strongly on temperature and pressure. All other thermodynamic and transport properties are also functions of temperature and pressure. Thus to compute the eigen vector matrices, the Jacobean matrix $\frac{\partial \mathbf{F}}{\partial \mathbf{U}}$ needs to be recomputed. Here $\mathbf{F}$ denotes the flux vector and $\mathbf{U}$ denotes the vector of the conserved variables.

The Jacobian matrix is computed as

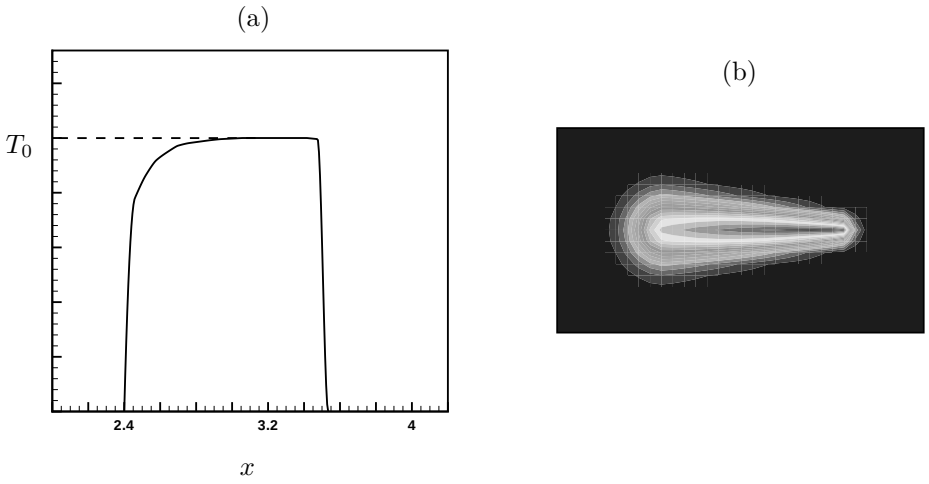

Figure 3. (a) Axial variation of the initial temperature profile, (b) Contour plot of initial temperature in a plane through the plasma axis.

$$\mathbf{J} = \begin{pmatrix} 0 & 1 & 0 & 0 \\ (-u^2 + \frac{1}{\theta_1}(RT - G_1 - A(e - e_k))) & (2 - \frac{A}{\theta_1})u & -\frac{A}{\theta_1}v & -\frac{A}{\theta_1}w & \frac{A}{\theta_1} \\ -vu & v & u & 0 & 0 \\ -wu & w & 0 & u & 0 \\ -(A'(e - e_k) + e_0 + G_1 + G_1G_2 - RTG_2) & (e_0 + RT - A'u^2) & -A'uv) & -A'uw) & (1 + A')u \end{pmatrix}$$

where,

$$A' = 1 + A, \quad G_1 = \frac{Ap}{\theta_1}\frac{\partial e}{\partial p}, \quad G_2 = \frac{\rho T}{\theta_1}\frac{\partial R}{\partial p} \tag{18}$$

and

$$A = (R + T\frac{\partial R}{\partial T})\frac{1}{\theta_2}, \quad \theta_1 = (1 - \frac{p}{R}\frac{\partial R}{\partial p}), \quad \theta_2 = \frac{\partial e}{\partial T} + \frac{\partial e}{\partial p}\left(\frac{\frac{p}{T} + \frac{p}{R}\frac{\partial R}{\partial T}}{1 - \frac{p}{R}\frac{\partial R}{\partial p}}\right) \tag{19}$$

This matrix was reconstructed based on the assumption that the thermodynamic properties are functions of pressure and temperature. Note that this is easily reducible to the case where only temperature variation of the thermodynamic properties are considered. The gradients of e and R with respect to pressure are assumed to be negligible.Hence,

$$G_1 = G_2 = 0, \quad \theta_1 = 1, \quad \theta_2 = \frac{de}{dT}, \quad A' = (R + T\frac{\partial R}{\partial T})\frac{dT}{de}. \tag{20}$$

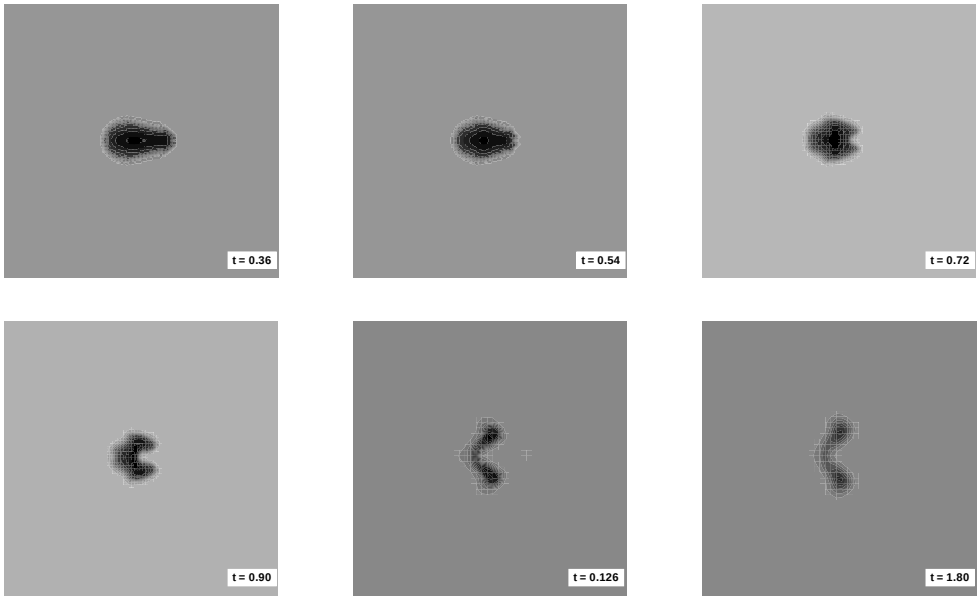

Figure 4. Plots of temperature contours showing evolution of the temperature field in time.

This can be further be reduced to the low temperature case where the specific heats are constant and the thermodynamic properties can be obtained using explicit relations(equations 7 and 8). Then A further simplifies to

$$A = (\gamma - 1). \tag{21}$$

The Jacobian matrix then reduces to its standard low temperature form. The eigen vector matrices can be computed from the Jacobian matrix following an eigen value analysis.

IV. Laser–induced breakdown in quiescent air

Experiments in laser induced breakdown (Adelgren et al 2001, Yan et al 2003) show that the plasma is initially tear–drop shaped. Figure 3a shows the axial temperature distribution that is used to model the initial temperature profile of the plasma. This temperature distribution is obtained from simulations of Kandala (2005) who models the initial plasma formation in detail. Laser energy deposition is symmetric about the laser axis. The temperature profile normal to the plasma axis is assumed to be a Gaussian. The ratio of the maximum temperature in the plasma core to the background temperature, T_0, determines the amount of laser energy absorbed by the flow. Figure 3b shows contours of initial temperature in a plane passing through the axis of the plasma.

A. Results for $T_0 = 30$

This section contains simulation results for $T_0 = 30$ obtained using model 3 described in section II, subsection C. All results are shown in nondimensional units. The reference length scale ${L_0}^*$ and reference time scale ${t_0}^*$ (section II) are 5.55 mm and 15.99 μs respectively and can be used to convert the results into dimensional quantities. The dimensional plasma length used is 6.3 mm (Kandala 2005). The reference values for temperature, pressure and density are 300 K, 1 $atmosphere$ and 1.2 Kg/m^3 respectively.

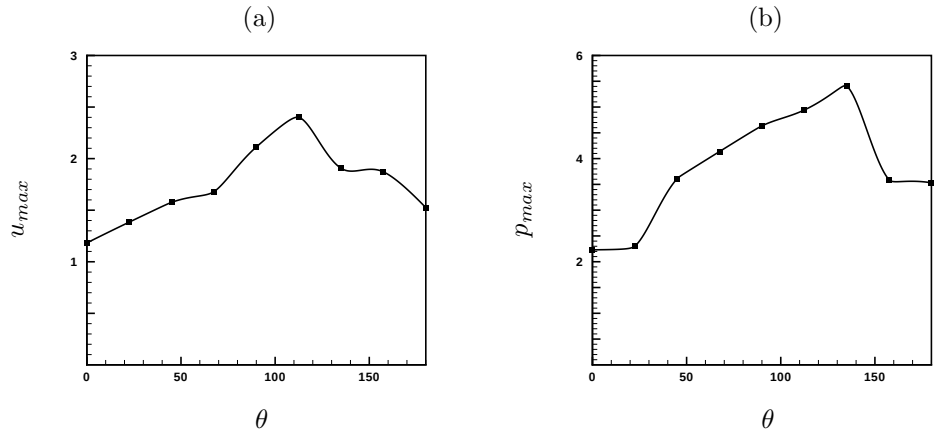

Figure 5. (a) Angular variation of velocity magnitude at the shock front at $t = 0.06$ when the shock intensity is maximum, (b) Angular variation of pressure at the shock front at that instant of time.

The flow field resulting from laser energy deposition is described in detail in this section. Energy deposition results in formation of a blast wave that propagates into the background. Due to the initial shape of the plasma region, the blast wave is initially tear–drop shaped, but becomes spherical in time. Figure 4 shows a long–time evolution of the temperature field obtained in the simulations. Note that the temperature field starts breaking up around $t = 0.54$. The break–up starts in the form of a dent on the right, along the axis of the plasma. This dent propagates along the plasma axis from right to left resulting in formation of an axisymmetric temperature lobe around $t = 0.90$. In time, this temperature lobe moves further away from the plasma axis and finally rolls up to form a toroidal vortex ring as shown in the contours of temperature at $t = 1.80$. Note that during this process, the maximum temperature is advected from the plasma axis to the center of the vortex ring. The breaking and roll–up of the plasma core observed in this figure is a characteristic feature of the flow that has been observed in experimental flow visualization (Adelgren 2003, Glumac 2005).

1. Shock formation and propagation.

When laser energy is deposited in air, a part of it is absorbed as internal energy of the air molecules. This results in a localized hot energy spot. Since the energy deposition process is very fast, the gas density does not change significantly during this period. Hence sharp gradients in temperature and pressure are developed within the energy spot. These gradients act as sources of acceleration on the right hand side of the Navier–Stokes equations, and generate fluid motion. Thus the internal energy of the fluid elements is converted into kinetic energy and a shock wave begins to form. This process continues until the shock front attains a maximum intensity. Then the shock wave propagates into the background, and its strength decreases as a result.

As the shock wave develops, a distinct asymmetry in shock strength is observed along the length of the plasma spark. The preferred direction is the direction normal to the plasma axis and the shock wave is strongest in this direction. As the shock wave propagates into the background, it loses its preference for the normal direction and becomes more spherical over time. The sharp gradients in pressure normal to the plasma axis result in strong fluid acceleration and hence the shock radius increases faster in this direction. Thus the shock wave starts looking more spherical in time. Also the shock strength become more and more uniform in all directions.

Figure 5a shows the angular variation of velocity magnitude at the shock front at the instant when the shock is strongest. Figure 5b shows the angular variation of pressure at the shock front at the same instant. Here,

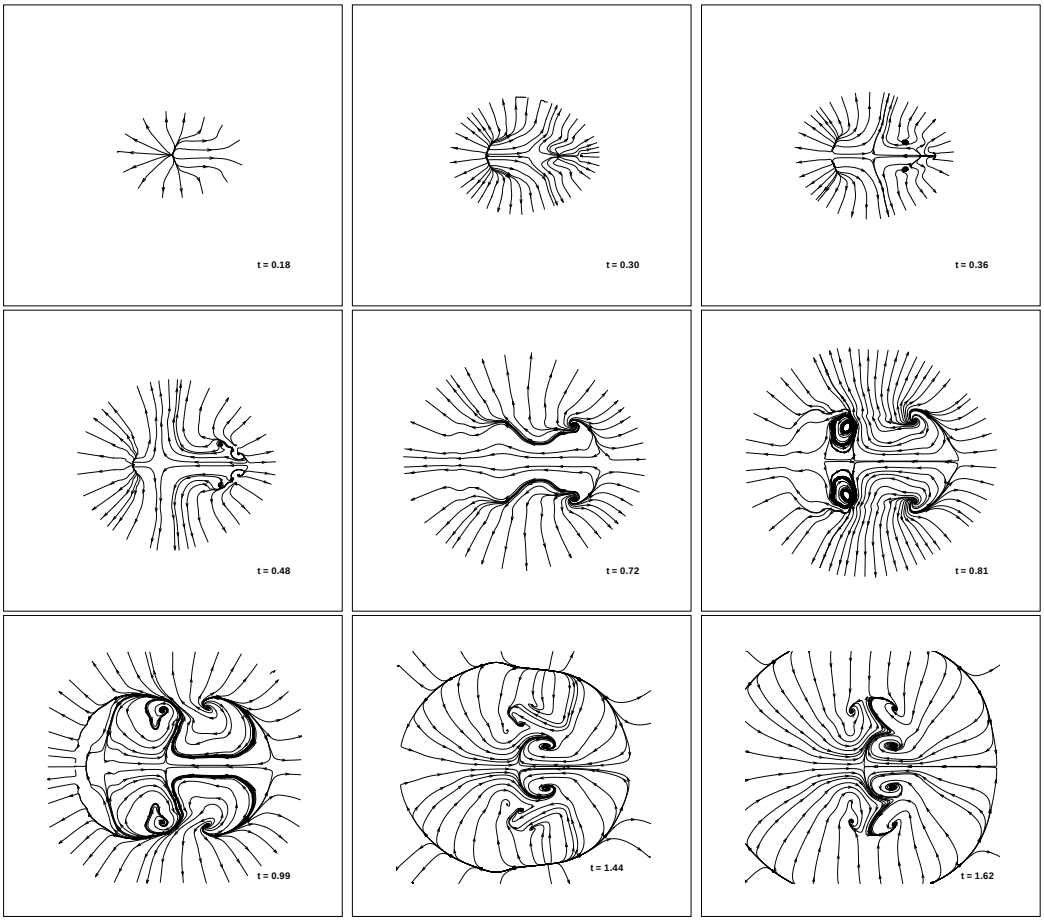

Figure 6. Plots of velocity streamlines showing evolution of the flow field in time.

the angle θ is defined with respect to the plasma center and measured away from the plasma axis from right to left. Note that the maximum shock strength is around $\theta = 135^0$ and not at the center. This is because the pressure field varies axially as well. Figure 3a shows the initial axial profile of the temperature field. In time, the peak of the temperature profile is advected towards the left due to a combined effect of its its axial and radial asymmetry. Thus normal pressure gradients are stronger for $\theta > 90^0$.

2. Roll up of the plasma core.

As the shock wave propagates outwards, the temperatures in the plasma core decay in an interesting manner. Note that the initial axial temperature profile has a single peak (figure 3a). In time this peak advects to the left due to a combined effect of its its axial and radial asymmetry of the problem. This results in a single center of expansion as observed in plots of velocity streamlines at $t = 0.18$ (figure 6). However in time the temperatures in the plasma core decay in a manner such that the axial temperature profile splits to form two independent centers of expansion ($t = 0.30$). This behavior is also observed in Glumac et al.'s (2005) experiments (figure 8 of their paper). The second expansion point is initially weaker than the first, but as the core temperatures continue to decay in magnitude, the two expansion points become comparable in strength ($t = 0.36$). Since the temperatures decay faster near the first expansion point soon the second

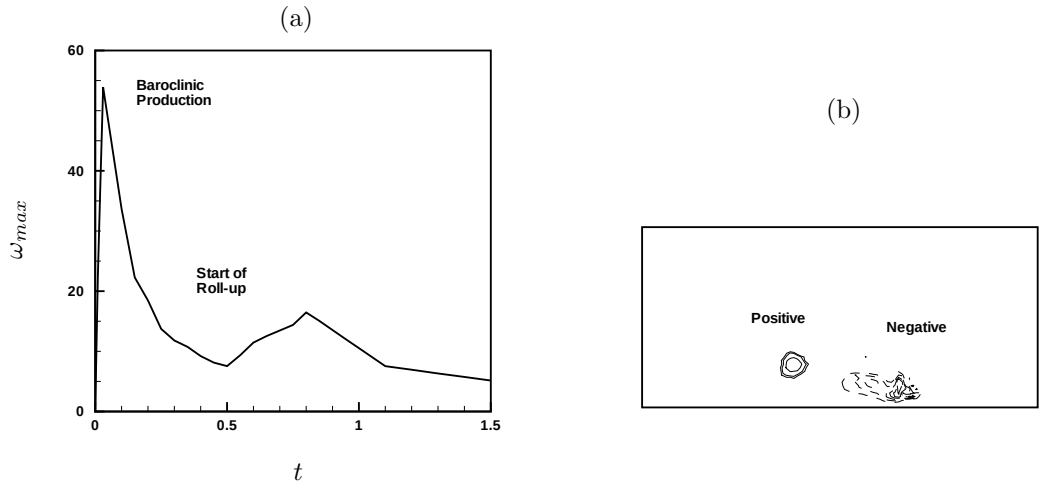

Figure 7. (a) Evolution of maximum vorticity magnitude in time, (b) Baroclinic vorticity contours at $t = 0.18$ show generation of vorticity near the leading and trailing edges of the plasma.

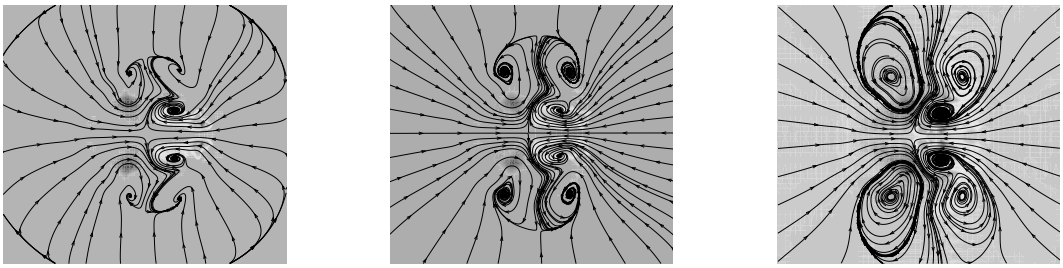

Figure 8. Velocity streamlines plotted over contours of vorticity magnitude at $t = 1.60$, $t = 2.0$ and $t = 2.40$.

expansion point becomes much stronger than the first and fluid rushes in from right to left thus running over the first expansion point ($t = 0.48$). The reverse flow results in sharp acceleration of the fluid elements along the plasma axis. Interaction of the fluid elements rushing in from the right with those coming out of the first expansion point results in sharp turning of the flow normal to the plasma axis and hence in the flow getting separated forming complicated vortices. These vortices evolve in time to form a series of complex vortex structures (figure 6) finally resulting in formation of the toroidal vortex ring observed in experiment (Adelgren 2003, Glumac 2005).

Note that as the plasma is initially expanding, the flow along the plasma axis is from left to right. However in time the direction of flow along the axis is reversed. As the reverse flow builds up in strength, it becomes stronger than even the velocity at the shock front. This reverse flow is responsible for the vortex structures that are developed in the flow.

3. Vorticity generated in the flow

Vorticity is observed to be generated in the flow by different processes at different times. Figure 7a shows time evolution of maximum vorticity generated in the flow. At short times ($t < 0.30$), baroclinic production is observed to be the dominant source of vorticity in the flow while at longer times the collapse of the plasma

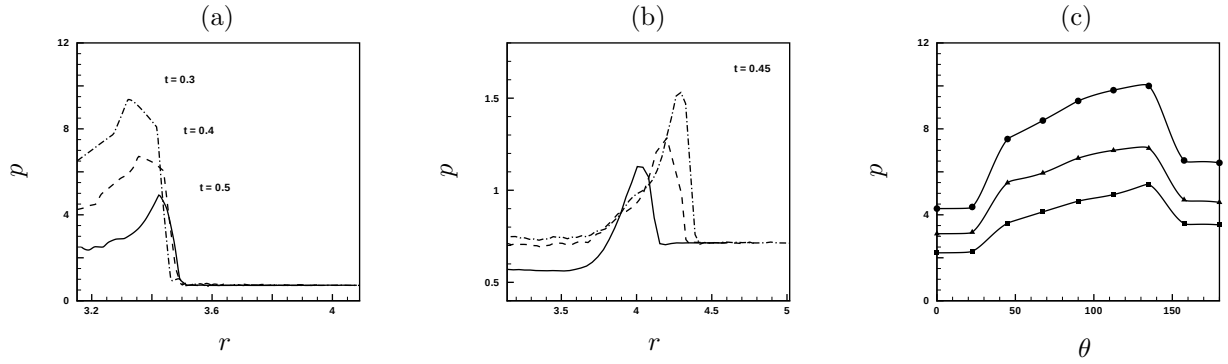

Figure 9. (a) Radial pressure profiles ($\theta = 90^0$) for $T_0 = 30$(———), $T_0 = 36$(- - - -) and $T_0 = 42$(—·—) at the end of shock formation for each case, (b) Radial pressure profiles ($\theta = 90^0$) for $T_0 = 30$(———), $T_0 = 36$(- - - -) and $T_0 = 42$(—·—) at $t = 0.45$, (c) Angular variation of pressure at the shock front at the instant when it is maximum, ■ : $T_0 = 30$, ▲ : $T_0 = 36$, ● : $T_0 = 42$.

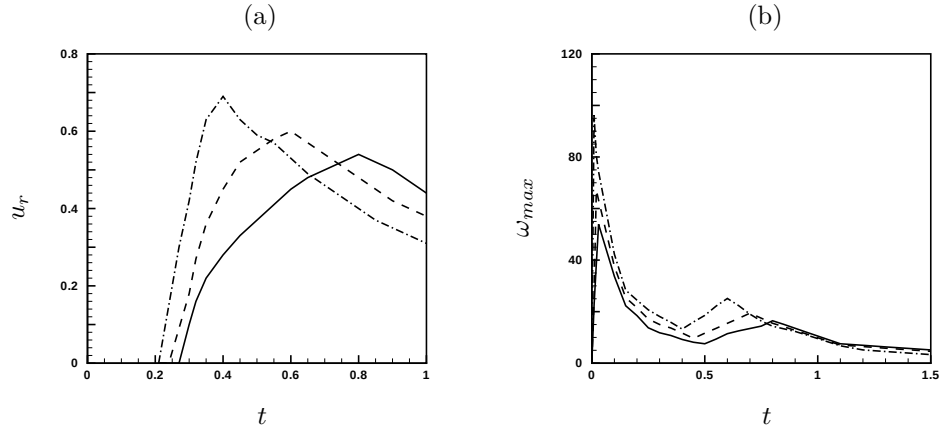

Figure 10. (a) Time evolution of the maximum reverse flow magnitude for different T_0, (b) Time evolution of the maximum vorticity magnitude for different T_0, ——— : $T_0 = 30$, - - - - : $T_0 = 36$ and —·— : $T_0 = 42$.

core described in the previous section results in generation of vorticity in the flow.
The baroclinic vorticity is observed near the leading and trailing edges of the plasma. Figure 7b shows contours of vorticity magnitude at a given instant of time. These contours are shown in a plane passing through the axis of the plasma. Positive and negative vorticity is observed near the leading and trailing edges of the plasma. Vorticity generation is stronger near the leading edge. The magnitude of vorticity is observed to decrease in time, as it spreads out further from the core of the plasma. At long times, vorticity is generated due to the collapse of the plasma core. This vorticity generation process has been described in detail in section IV, subsection A2. The actual vorticity field is much more complicated than just a single toroidal vortex ring as observed in experiments of laser–induced break down (Adelgren et al 2001). However the magnitude of vorticity is much stronger in the vortex ring closest to the plasma axis. This can be shown by plotting velocity streamlines over contours of vorticity magnitude (figure 8). Thus only a single toroidal vortex ring is observed in the experimental flow visualization.

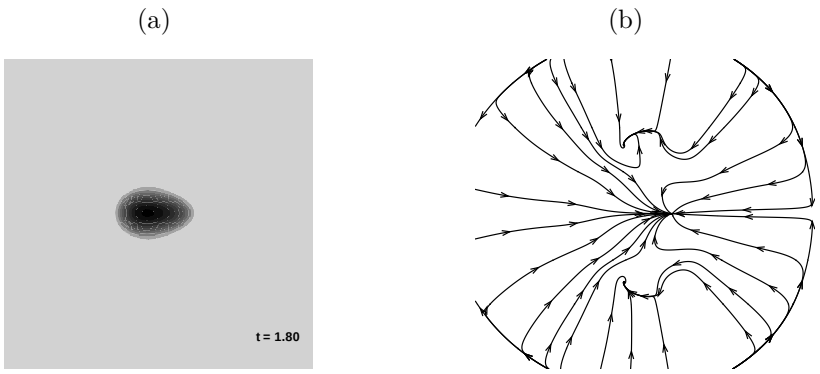

Figure 11. (a) Temperature contours and (b) Velocity streamlines at $t = 1.80$ show that for Re $= 1200$ the core of the plasma does not roll–up in time.

B. Parametric study

Recall that the relevant parameters associated with the problem are the shape and size of the initial plasma region, the maximum temperature ratio in the plasma core T_0 and Reynolds number of the flow. The effects of change in T_0 and the Reynolds number on the resulting flow field are discussed in the following sections. All simulations in this section use model 3 described in section II, subsection C.

1. Effect of T_0

The shape and size of the initial plasma region is same as that used for the previous simulations and is assumed to be independent of T_0 over the range for which the simulations are performed. Results are shown for $T_0 = 30$, 36 and 42. Viscosity for air is computed under conditions of equilibrium as discussed in section II.

Higher the value of T_0, stronger are the initial gradients in the pressure field. Hence a stronger shock wave develops with increase in T_0. Figure 9a shows radial profiles for pressure computed normal to the plasma axis at the end of shock formation. Note that the maximum intensity for the developed shock wave is highest for $T_0 = 42$. Also, note that the shock formation time is smallest for $T_0 = 42$ and largest for $T_0 = 30$. The process of conversion of internal energy into kinetic energy is also faster with increase in energy deposited. Since the pressure gradients are strongest for $T_0 = 42$, higher shock velocities are developed in this case. Thus, if profiles are compared at the same instant of time, the shock wave for $T_0 = 42$ will have propagated further out into the domain when compared to the other two temperatures. This behavior is shown in figure 9b. Radial profiles for pressure computed normal to the plasma axis at $t = 0.45$ are shown for different T_0. The shock radius is observed to be largest for $T_0 = 42$ and smallest for $T_0 = 30$. Figure 9c shows angular variation of pressure at the shock front at the end of the shock formation process. The angle θ is defined as described in section IV, subsection A1. Note that the shock strength increases with increase in T_0 but for a given T_0, the angular spread of the shock strength does not change much.

Figure 10a shows evolution of the maximum reverse flow magnitude u_r in time for different T_0. Note that for higher T_0, stronger reverse flows are obtained. However, the overall trend remains same for different T_0. Recall that this reverse flow was found to be responsible for generating vorticity in the flow at long times. Figure 10b shows evolution of the maximum vorticity magnitude in time for different T_0. Stronger the reverse flow developed, higher is the magnitude of vorticity generated. Also the baroclinic vorticity generated at short times is observed to be stronger for higher T_0. This is because the baroclinic vorticity generated depends directly on the local shock strength which increases with increase in T_0. Also note that

the process of setting up of the reverse flow and generation of vorticity in the flow speeds up with increase in T_0.
Table 1 provides a quantitative estimate for how the flow varies with T_0. All quantities are nondimensional as discussed in section II. Also, the shock formation time is obtained based on maximum pressure gradients at the shock front. The time at which roll–up begins is defined as the instant when $u/u_s = 0.01$.

2. Effect of Reynolds number

The Reynolds number **Re** is defined in section II and is obtained as 1.27×10^5. **Re** is computed using the values for the length of the plasma region, density of air and the reference temperature stated in section IV, subsection A and viscosity of air $\mu = 1.73 \times 10^{-5}\ Ns/m^2$. The effect of **Re** on the flow is discussed in this section.
Figure 11a shows temperature contours at $t = 1.8$ and **Re** $= 1200$. Comparison to the time evolution of the temperature field shown in figure 4 shows that the core of the plasma does not roll–up for low **Re**. Figure 11b shows velocity streamlines obtained at the same instant of time. Note that fluid elements move in along the plasma axis from both directions and do not turn normal to the plasma axis. Comparison to the velocity stream lines shown in figure 6 indicates that the sequential evolution of the velocity field that eventually results in rolling up of the plasma core does not occur for the low **Re** case. These results can be attributed to enhanced viscous dissipation resulting from the decrease in **Re**. Note that the effect of numerical dissipation will be similar, and so it is important to minimize numerical dissipation in such simulations.

C. Comparison between different models

The objective of this section is to investigate as to what minimum level of physical complexity would be required for a model to predict breaking and roll up of the core. This section also tries to discuss how adding different physical aspects to the model influence the initial conditions and the time evolution of the resulting flow field. Results obtained from three different simulation models are compared. For the first model, the effects of chemical reactions are neglected. In other words all the properties for air have been assumed to be constant. For the second model, the effect of temperature variation on the thermodynamic and transport properties of air are considered. For the third model, the effect of both temperature and pressure variation on the properties of air are accounted for. The details of the simulation methodology used for the different models have been discussed in section II.
All simulations in this section are conducted for $T_0 = 30$. Figure 12 shows the initial pressure profiles obtained for the three different models. Note that the maximum initial pressure obtained is significantly different for the three models. For all the three models, the initial pressure profile is obtained from the relation

$$p^* = \rho^* R^* T^*, \tag{22}$$

T_0	*Maximum initial pressure*	*Maximum velocity at shock front*	*Maximum baroclinic vorticity*	*Maximum vorticity due to roll up*	*Shock formation time*	*Roll up begin time*
30.0	35.23	2.40	53.90	16.46	0.05	0.27
36.0	49.65	2.73	67.20	19.41	0.04	0.24
42.0	61.67	3.35	96.20	25.12	0.03	0.21

Table 1. Effect of T_0 on different flow quantities.

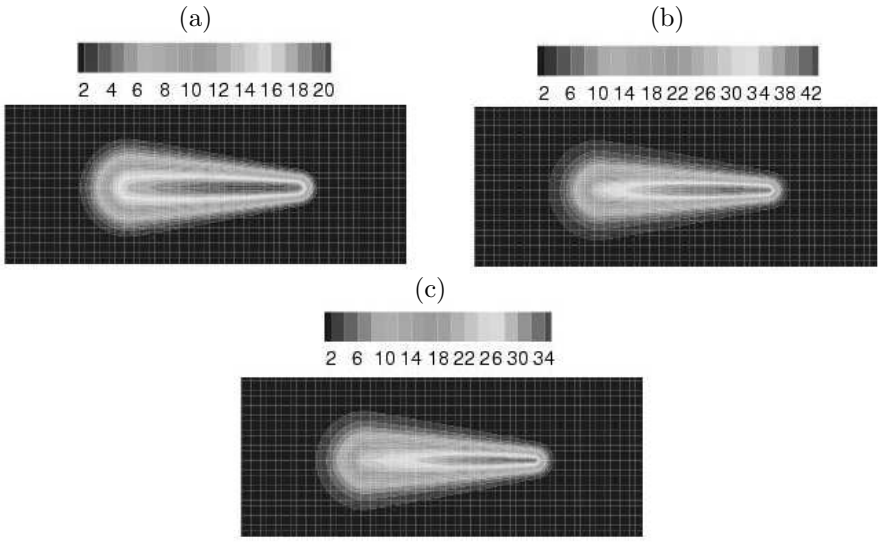

Figure 12. Initial pressure contours obtained for three different models, (a) model 1, (b) model 2 and (c) model 3.

used in a suitable nondimensional form. For the first model $R^* = {R_0}^*$ and is a constant. So the pressures obtained are significantly low. For the second model, due to the effect of chemical reactions, the value of R^* at higher temperatures is significantly greater than ${R_0}^*$ (figure 2c). Thus the initial pressures are much higher in this case. For the third model, with increase in pressure, the value of R^* is found to decrease at higher temperatures (figure 2c). Thus the initial pressures in this case are intermediate between the other two models.

Table 2 provides a quantitative estimate for how different flow variables vary with the simulation model used. All quantities are in nondimensional form (section II). Since the initial pressure gradients drive the flow, the results obtained from the different models would scale similar to those obtained by changing T_0. Figure 13a shows angular variation of pressure at the shock front at the end of shock formation. Note that from one model to another, the profiles look very similar. However, their levels are quiet different. Highest pressures are obtained for the second model and lowest pressures are obtained for the first model. Figure 13b shows radial pressure profiles computed normal to the plasma axis at $t = 0.45$. The shock front is observed to be weakest and the shock radius minimum for the first model while the reverse is true for the second model.

The evolution of the flow field is observed to be qualitatively similar for all the three models. Figure 14 compares velocity streamlines from the different models at the same instant of time. Since for the first model the initial pressure gradients are the weakest, the flow field evolves slowly when compared to the other cases.

Model ($T_0 = 30$)	*Maximum initial pressure*	*Maximum velocity at shock front*	*Maximum baroclinic vorticity*	*Maximum vorticity due to roll up*	*Shock formation time*	*Roll up begin time*
1	21.07	1.69	28.45	12.06	0.06	0.30
2	42.89	2.87	63.78	18.81	0.04	0.25
3	35.23	2.40	53.90	16.46	0.05	0.27

Table 2. Variation of different flow quantities with the simulation model used.

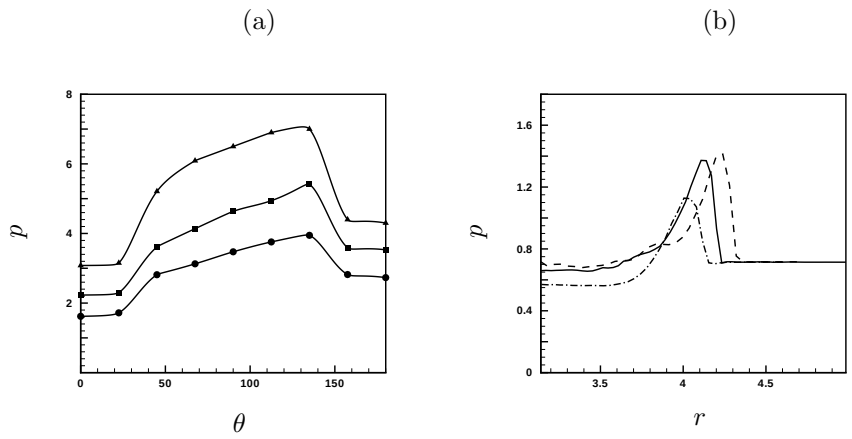

Figure 13. (a) Angular variation of pressure at the shock front at the instant when it is maximum, ● : model 1, ▲ : model 2, ■ : model 3, (b) Radial pressure profiles ($\theta = 90^0$) for model 1 (—·—), model 2 (- - - -) and model 3 (———) at $t = 0.45$.

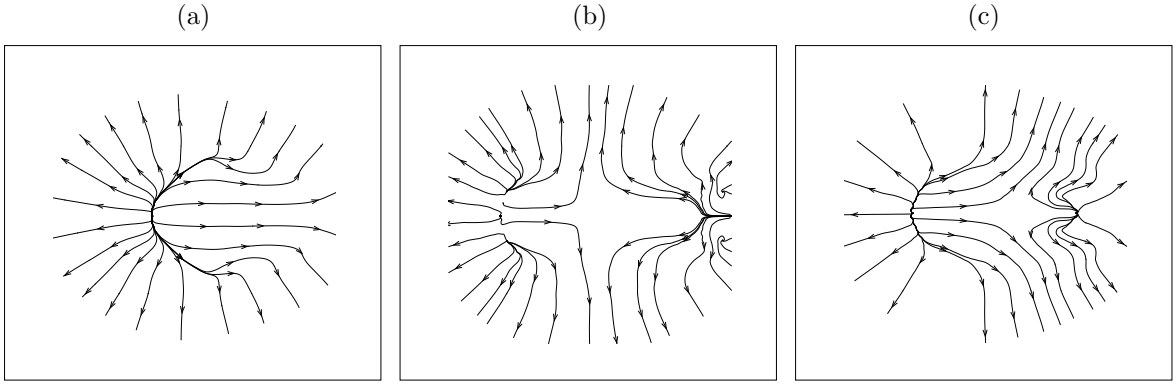

Figure 14. Comparison of velocity streamlines from different models at $t = 0.3$, a) model 1, (b) model 2 and (c) model 3.

For the second model, the flow field evolves faster than the other cases. Note that all the three figures are at different stages of the characteristic flow evolution sequence shown in figure 6. Figure 14a shows that at $t = 0.3$ only a single expansion center is observed. Figure 14b shows that the flow has evolved to a much later stage where two distinct expansion centers of comparable strength are observed. Figure 14c shows that the flow field has evolved to a stage intermediate between the other two cases. The flow field is observed to eventually roll–up for all the three models. Even an ideal gas representation is sufficient to predict the roll–up of the plasma core. However the results are quantitatively different and are found to scale with the amount of initial energy added to the flow. It is important to note that this scaling is similar to, but not same as that obtained in the previous section where only the third model is used and T_0 is varied. This is because for the different models, both the initial conditions and the time evolution of the flow are different. In other words, the initial pressure profiles are not the only factor influencing the evolution of the flow field.

V. Laser–induced breakdown in isotropic turbulence

As described in section IV, the main characteristics of the flow resulting from laser–induced breakdown of air are expansion in the plasma core, formation and propagation of a blast wave of varying strength and curvature through the background, and rolling up of the plasma core in time. This section describes the effect of these processes on background isotropic turbulence.

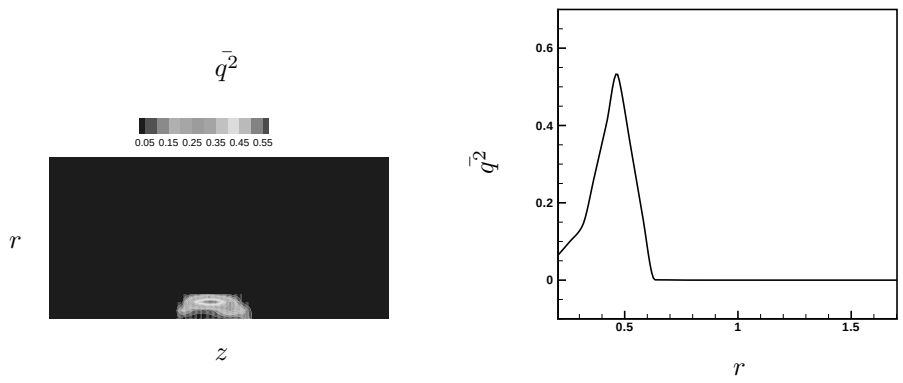

Figure 15. Statistics for turbulent kinetic energy at $t = 0.15$, (a) axis-symmetric, (b) radial profile at $z = 3.14$ (center of the domain).

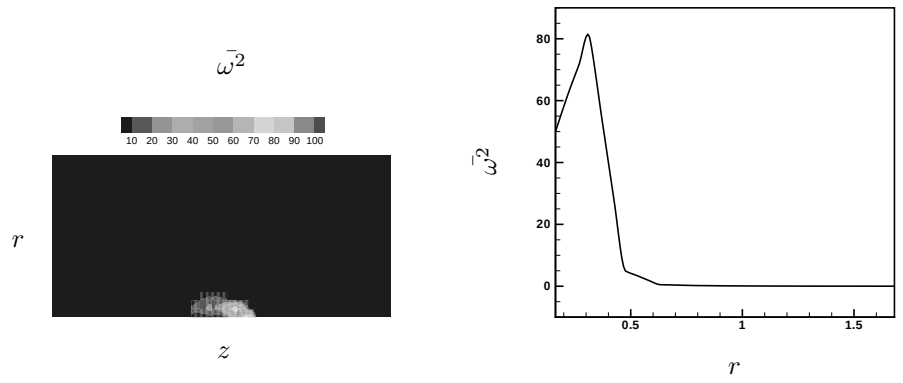

Figure 16. Statistics for vorticity fluctuations at $t = 0.15$, (a) axis-symmetric, (b) radial profile at $z = 3.4$ (near the leading edge of the initial plasma region).

The turbulent initial conditions are generated using Rogallo's (1981) method. The initial velocity fluctuations are isotropic and divergence–free, while initial fluctuations in pressure, temperature and density are assumed to be zero. The initial energy spectrum used in the simulations is a power four spectrum peaking at $k_0 = 5$. The initial flow field thus generated has a turbulent Reynolds number $Re_\lambda = 50$. The simulations are conducted on a 300^3 point mesh so that the dissipation spectrum is well–resolved. A fluctuation Mach number $M_t = 0.001$ is chosen to create conditions similar to experiments of Comte–Bellot Corrison (1971). Note that there is a big difference between the time–scales of the mean flow and that of the background turbulence.

The turbulent field is allowed to decay for some time after which the velocity derivative skewness attains a steady value in the range of -0.3 to -0.4. Laser energy is then added to this flow by locally increasing the temperature and pressure at constant density.

A. Results for $T_0 = 30$

This section contains simulation results for $T_0 = 30$ obtained using model 3 described in section II, subsection C. As a result of laser energy deposition, a very strong blast wave propagates into the background,

Figure 17. Long time vorticity generation due to roll–up of the plasma core, (a) velocity streamlines plotted over contours of vorticity magnitude at $t = 1.2$, (b) vorticity contours at $t = 1.2$.

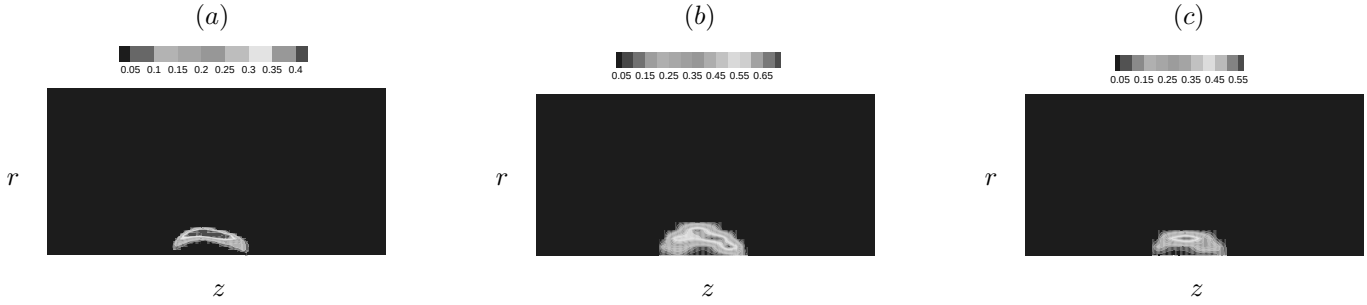

Figure 18. Axis-symmetric statistics for turbulent kinetic energy at $t = 0.15$, (a) model 1, (b) model 2, (c) model 3.

compressing the turbulence, leaving the flow in the core to expand. The blast wave is initially strong and hence retains its tear drop shape. But the effect of the background turbulence is to dampen the blast wave intensity and soon it becomes weak enough to interact noticeably with the turbulence and its shape gets distorted.

Compression across the blast wave affects turbulence levels in its vicinity. Note that the turbulence is statistically homogeneous in axisymmetric planes with respect to the plasma axis. Statistics were therefore computed in $z - r$ planes. Figure 15a shows statistics for turbulent kinetic energy at $t = 0.15$. Note that in the vicinity of the blast wave turbulence levels are amplified due to mean compression. This trend is supported by linear analysis of turbulence interacting with a shock wave (Mahesh et al. 1995,1997). A vertical slice is extracted from figure 15a at the center of the domain ($z = 3.14$) and shown in figure 15b. The extent of turbulence amplification across a shock wave depends on the local strength of the shock wave. Figure 16a shows statistics for vorticity fluctuations $\overline{\omega^2}$ at $t = 0.15$. Note that the vorticity fluctuations get amplified near the leading and trailing edges of the initial plasma region i.e. in regions where the mean vorticity levels were found to be high due to baroclinic production of vorticity at short times. Figure 16b shows a vertical slice extracted from figure 16a at a section near the leading edge of the plasma ($z = 3.4$) and plotted as a function of distance perpendicular to the plasma axis.

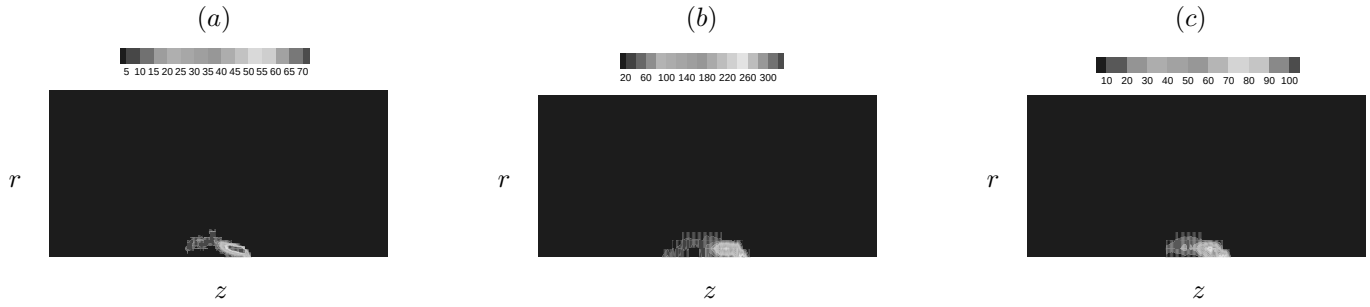

Figure 19. Axis-symmetric statistics for vorticity fluctuations at $t = 0.15$, (a) model 1, (b) model 2, (c) model 3.

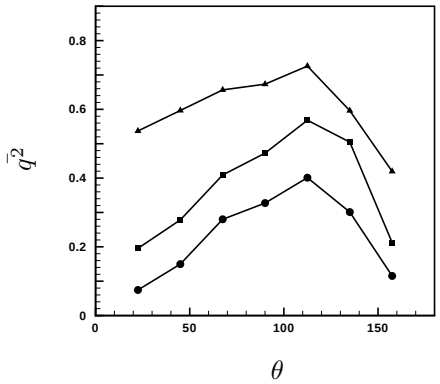

Figure 20. Angular variation of the turbulent kinetic energy amplification across the shock wave at $t = 0.15$, ● : model 1, ▲ : model 2, ■ : model 3 .

Recall that the mean flow generates vorticity at long times due to rolling up of the plasma core (section IV, subsection 3). This enhances the vorticity levels of the turbulent background near the plasma core. Figure 17a shows velocity streamlines plotted over contours of vorticity magnitude at $t = 1.2$. Figure 17b shows vorticity contours only at that instant of time. Note that since the turbulence in the background is very weak it does not affect the evolution of the mean flow significantly. Hence the core of the plasma region rolls up in time adding vorticity to the flow. Also note that the vorticity generated by the rolling up process is much stronger compared to the vorticity of the background flow.

B. Comparison between different models

The effect of the different simulation models (section II) on turbulence is discussed in this section. Recall that the initial pressure profiles (section IV, subsection C) indicate that maximum initial pressures are obtained for the second model while minimum initial pressures are obtained for the first model. Since the mean flow is driven by pressure gradients and since the effect on the turbulent fluctuations would be proportional to the strength of the mean flow, maximum modification of the turbulence levels is observed for the second model while minimum modification is observed for the first model.
Figure 18 shows axisymmetric plots for turbulent kinetic energy obtained from all three models at $t = 0.15$. Note that maximum amplification of turbulent kinetic energy in the vicinity of the blast wave is observed for model 2 and minimum amplification is observed for model 1. Similar plots are shown (figure 19) for vorticity fluctuation statistics $\bar{\omega^2}$ obtained from the three different models. Again maximum amplification

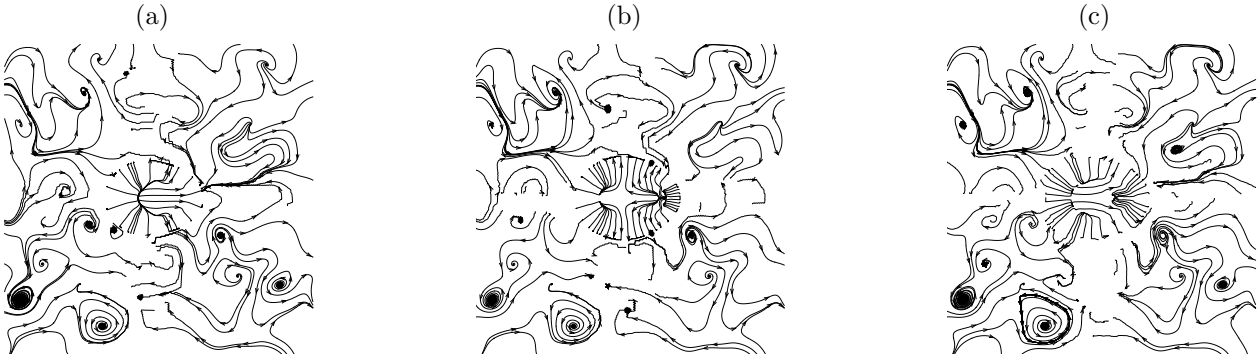

Figure 21. Comparison of velocity streamlines from different models at $t = 0.3$, a) model 1, (b) model 2 and (c) model 3.

in vorticity levels is observed for model 2 and minimum amplification is observed for model 1. Statistics obtained using model 3 show the amplification in this case is intermediate between that obtained from the other two models.

Since at any given instant of time the blast wave varies in strength and curvature, the turbulent kinetic energy amplification across it also has an angular variation. Figure 20 shows variation of turbulent kinetic energy with angle θ defined in section IV, subsection A1. Note that for any given model, the amplification in turbulent kinetic energy peaks for $\theta > 90^0$. Again amplification levels are maximum for model 2 and minimum for model 1.

Figure 21 compares velocity stream lines obtained from models 1,2 and 3 respectively at $t = 0.3$. A comparison between figures 21 and 14 shows that the turbulence in the background is weak compared to the blast wave and so the mean flow evolves without getting much affected by the turbulence in the background. As discussed in section IV, subsection C, the core of the plasma region eventually rolls up for all the three different models. However the time required for roll up is minimum for model 2 and maximum for model 1. Also vorticity generated due to roll up is strongest for model 2 and weakest for model 1.

VI. Summary

This paper uses numerical simulation to study the effect of laser energy deposition on quiescent air. Local thermodynamic equilibrium conditions are assumed to apply. The simulations solve the compressible Navier–Stokes equations using Fourier spectral methods. A predictor–corrector based shock capturing scheme is incorporated to account for the strong shock waves. Three different models have been used to obtain the thermodynamic and transport properties for air. For the first model, the effect of the chemical reactions have been neglected and so the properties are assumed to be constant. For the second model, the properties are assumed to vary with temperature only. However, the initial pressures obtained in the problem are very high and so pressure variation of these properties also need to be accounted for. The third model accounts for both temperature and pressure variation of the properties of air. For each different model, the corrector step of the shock capturing scheme have been suitably modified. Also, a logarithmic formulation for the continuity equation is developed to handle low densities at the core of the plasma.

Time evolution of the flow field is classified into formation of a shock wave, its propagation into the background and subsequent collapse of the plasma core. Each phase is studied in detail. Vorticity is found to be generated in the flow through different mechanisms at short and long times. At short times, vorticity is found to be generated by baroclinic means. At longer times, vorticity is generated as a result of the reverse flow in

the plasma core. Scaling analysis is performed for different amounts of laser energy deposited and different Reynolds number. Jumps at the shock front are found to scale with the initial pressure gradients and hence with the amount of energy deposited in the flow. However, the propagation of the shock wave and formation of the reverse flow is found to be qualitatively similar for different amount of energy deposited. The plasma core does not roll–up for the low **Re** simulation. Results obtained from simulations conducted using three different models for air have been compared. The initial pressure fields are found to be significantly different for the three models. Again, the results are found to scale with the initial gradients in the pressure field. However, for each model, the flow field is found to evolve in a qualitatively similar manner.
For the turbulent simulations, amplification in turbulence levels are observed in the vicinity of the blast wave due to presence of local compression. Vorticity levels are observed to amplify near the leading and trailing edges of the plasma due to baroclinic effects at short times and in the plasma core at long time due to rolling up of the core. Different models for the plasma are used to study the effect on turbulence. The effects on background turbulence are found to scale with the initial pressure gradients.

Acknowledgments This work is supported by the United States Air Force Office of Scientific Research under grant FA-9550-04-1-0064. Computing resources were provided by the Minnesota Supercomputing Institute, the San Diego Supercomputing Center, and the National Center for Supercomputing Applications.

References

[1]R.G. Adelgren, H. Yan, G.S. Elliot, D. Knight, T.J. Beutner, A. Zheltovodov, M. Ivanov & D. Khotyanovsky, 2003, Localized flow control by laser energy deposition applied to Edney IV shock impingement and intersecting shocks, *AIAA paper 2003–31*.

[2]R. Adelgren, M. Boguszko & G. Elliott, 2001, Experimental summary report–shock propagation measurements for Nd:YAG laser induced breakdown in quiescent air, Department of Mechanical and Aerospace Engineering, Rutgers University.

[3]G.A Blaisdell, N.N. Mansour and W.C Reynolds, 1991, Numerical simulations of compressible homogeneous turbulence, Report No TF-50, Thermosciences Division, Department of Mechanical Engineering, Stanford University.

[4]H.L. Brode, 1955, Numerical solution of blast waves, *J. Appl. Phys.*, **26(6):** 766–775.

[5]Y. Chen, J. Lewis & C. Parigger, 2000, Spatial and temporal profiles of pulsed laser–induced air plasma emissions, *Journal of Quantitative Spectroscopy and Radiation Transfer*, **67:** 91–103.

[6]G. Comte–Bellot & S. Corrsin, 1971, Simple eulerian time correlation of full and narrow–band velocity signals in grid–generated 'isotropic' turbulence, *J. Fluid Mech.*, **48(2):** 273–337.

[7]E. Damon & R. Tomlinson, 1963, Observation of ionization of gases by a ruby laser, *Applied Optics*, **2(5)**.

[8]I. Dors, C. Parigger & J. Lewis, 2000, Fluid dynamic effects following laser–induced optical breakdown, *AIAA paper 2000–0717*.

[9]I.G. Dors & C.G. Parigger, 2003,Computational fluid–dynamic model of laser induced breakdown in air, *Applied Optics.*, **42(30)**.

[10]T. Ditmire, R. Smith, J Tisch & M. Hutchinson, 1997, High intensity laser absorption by gases of atomic clusters, *Physical review letters*, **78(16):** 3121–3124.

[11]S. Ghosh & K. Mahesh, 2005, Direct Numerical Simulation of the thermal effects in plasma/turbulence interaction, *AIAA paper 2007–0993*.

[12]N. Glumac, G. Elliott & M. Boguszko, 2005, Temporal and spatial evolution of the thermal structure of laser spark in air, *AIAA paper 2005–0204*.

[13]A. Harten, 1978, The artificial compression method for computation of shocks and contact discontinuities, *Math. Comp.*, **32**, 363.

[14]Z. Jiang, K. Takayama, K.P.B. Moosad, O. Onodera & M. Sun, 1998, Numerical and experimental study of a micro-blast wave generated by pulsed laser beam focusing, *Shock waves*, **8:** 337–349.

[15]N. Kroll & K. Watson, 1972, Theoritical study of ionization of air by intense laser pulses, *Physical Review A*, **5(4):** 1883–1905.

[16]R. Kandala, G. Candler, N. Glumac & G. Elliott, 2005, Simulation of laser–induced plasma experiments for supersonic flow control, *AIAA paper 2005–0205*.

[17]J. Lewis, C. Parigger, J. Hornkohl & G. Guan, 1999, Laser–induced optical breakdown plasma spectra and analyses by use of the program NEQAIR, *AIAA paper 99–0723*.

[18]K. Mahesh, S.K. Lele & P. Moin, 1995, The interaction of an isotropic field of acoustic waves with a shock wave, *J. Fluid Mech.*, **300:** 383–407.

[19]K. Mahesh, S.K. Lele & P. Moin, 1997, The influence of entropy fluctuations on the interaction of turbulence with a shock wave, *J. Fluid Mech.*, **334:** 353–379.

[20]P. Maker, R. Terhune & C. Savage, 1963, *Proccedings of the Third International Quantum Mechanics Conference*, Paris.

[21]R. Meyerand & A. Haught, 1963, Gas breakdown at optical frequencies, *Phys. Rev. Let.*, **11(9):** 401–403.

[22]P. Molina-Morales, K. Toyoda, K. Komurasaki & Y. Arakawa, 2001, CFD simulation of a 2–kW class laser thruster, *AIAA paper 2001–0650*.

[23]C. Parigger, D. Plemmons & J. Lewis, 1995, Spatially and temporally resolved electron number density measurements in a decaying laser–induced plasma using hydrogen –alpha line profiles, *Applied Optics*, **34(18):** 3325–3335.

[24]C. Parigger, J. Lewis & D. Plemmons, 1995, Electron number density and temperature measurement in a laser–induced hydrogen plasma, *Journal of Quantitative Spectroscopy and Radiation Transfer*, **53(3):** 249–255.

[25]T. X. Phuoc, 2000, Laser spark ignition: Experimental determination of laser–induced breakdown thresholds of combustion gases, *Optics Communications*, **175(4)**, 419–423.

[26]Y. P. Raizer, 1966, Breakdown and heating of gases under the influence of a laser beam, *Soviet Physics USPEKHI*, **8(5)**, 650–673.

[27]Yu. P. Raizer, 1997, *Gas discharge physics*, 2nd edition, Springer–Verlag, New York.

[28]D. W. Riggins, H.F. Nelson & E. Johnson, 1999, Blunt-body wave drag reduction using focused energy deposition, *AIAA J.*, **37(4)**, 460–467.

[29]R.S. Rogallo, 1981, Numerical experiments in homogeneous turbulence, *NASA Tech. Memo.* 81315.

[30]R. Root, 1989, Post breakdown phenomenon, *Laser–Induced Plasmas and Applications*.ed. L. J. Radziemski and D. A. Cremers, Marcel Dekker Inc., New York.

[31]M.N. Shneider, S.O. Macheret, S.H. Zaidi, I.G. Girgis, Yu. P. Raizer & R.B. Miles, 2003, Steady and unsteady supersonic flow control with energy addition, *AIAA paper 2003–3862*.

[32]H. Steiner, W. Gretler & T. Hirschler, Numerical solution for spherical laser–driven shock waves, *Shock waves*, **8:** 337–349.

[33]T. S. Wang, Y.S. Chen, J. Liu, L.N. Myrabo & F.B. Mead, 2001, *AIAA paper 2001–0648*.

[34]H. Yan, M. Adelgren, M. Bouszko, G. Elliott & D. Knight, 2003, Laser energy deposition in quiescent air, *AIAA paper 2003–1051*.

[35]S. Yalcin, D. Crosley, G. Smith & G. Faris, 1999, Influence of ambient conditions on laser air spark, *Applied Physics B*, **68:** 121-130.

[36]H.C. Yee, N.D. Sandham & M.J. Djomehri, 1999, Low–dissipative high–order shock–capturing methods using characteristic-based filter, *J. Comput. Phys.*, **150**, 199–238.

[37]Y. Zeldovich & Y. Raizer, 1965, Cascade ionization of gas by a light pulse, *Soviet Physics JETP.*, **20(3):** 772–780.